Path Integral Monte Carlo Study of Hydrogen Tunneling Effect on Dielectric Properties of Molecular Crystal 5-Bromo-9-hydroxyphenalenone

Hiroki Otaki[a,*], Koji Ando[b]

[a] *Theoretical Molecular Science Laboratory, RIKEN, 2-1 Hirosawa, Wako, Saitama 351-0198, Japan*
[b] *Department of Chemistry, Graduate School of Science, Kyoto University, Sakyo-ku, Kyoto 606-8502, Japan*

Abstract

The dielectric properties of proton(H)–deuteron(D) mixed crystals of the hydrogen-bonded material 5-bromo-9-hydroxyphenalenone are studied using a novel path integral Monte Carlo (PIMC) method that takes account of the dipole induction effect depending on the relative proton configurations in the surrounding molecules. The induced dipole is evaluated using the fragment molecular orbital method with electron correlation included by second-order Møller-Plesset perturbation theory and long-range corrected density functional theory. The results show a greater influence of $C-H\cdots O$ intermolecular weak hydrogen bonding on the induction than for results evaluated with the Hartree-Fock method. The induction correction is incorporated into the PIMC simulations with a model Hamiltonian that consists of long-range dipolar interactions and a transverse term describing proton tunneling. The relationship between the calculated phase transition temperature and H/D mixing ratio is consistent with the experimental phase diagram, indicating that the balance between the proton tunneling and the collective ordering is appropriately described.

Keywords: Molecular Crystal, Hydrogen Bonding, Dielectric Phase Transition, Isotope Effect, Monte Carlo Simulation

*Corresponding author
Email address: otaki@riken.jp (Hiroki Otaki)

1. Introduction

Ferroelectricity and antiferroelectricity are very important topics in condensed matter physics and chemistry. In particular, hydrogen-bonded materials that exhibit a large isotope effect on the phase transition temperature have attracted much attention. Representative inorganic materials are the potassium dihydrogen phosphate (KH_2PO_4) family, for which the paraelectric (PE)–(anti)ferroelectric ((A)FE) phase transition temperature is almost doubled by deuteration [1, 2].

In the field of organic electronics, significant progress has recently been made [3–9]. Horiuchi *et al.* reported several hydrogen-bonded organic ferroelectric materials, some of which exhibit a ferroelectric phase above room temperature [3, 5–7, 10–15]. Organic materials have the advantages of flexibility and variability in design. One of the main effective strategies for designing ferroelectric materials is to control the hydrogen bonding [14] involved in proton transfer, the isotope effect, and enhancement of spontaneous polarization.

5-Bromo-9-hydroxyphenalenone ($C_{13}H_7O_2Br$, BHP, see Figure 1), which belongs to the class of zero-dimensional hydrogen-bonded systems (intramolecular $O-H\cdots O$ bonds), also exhibits a prominent isotope effect. The deuterated compound (5-bromo-9-deuteroxyphenalenone; BDP) exhibits a PE–AFE phase transition via an incommensurate phase, while no phase transition has been observed down to 3 K in BHP [16–19]. From dielectric measurements, it has been suggested that a quantum paraelectric state is realized in BHP, in which the phase transition is suppressed by proton delocalization via tunneling in the intramolecular hydrogen bond. Although there is debate about the involvement of proton tunneling, the results of calorimetric, far-infrared spectroscopic, incoherent neutron scattering, and structural studies seem to support the quantum paraelectric state in BHP [20–23].

Compared with experimental studies, theoretical studies of hydrogen-bonded ferroelectric materials are rather scarce. A three-site model has been proposed to describe the isotope effect in zero-dimensional hydrogen-bonded (anti)ferroelectric materials [24]. More realistic quantum chemical calculations have been performed for several neighboring dimers of BHP and 5-iodo-9-hydroxyphenalenone [25, 26], in which the tunneling and interaction parameters were calculated to determine the ordered phase in the low-temperature limit using the mean field approximation. To complement these studies with the bulk properties of crystals, density functional theory

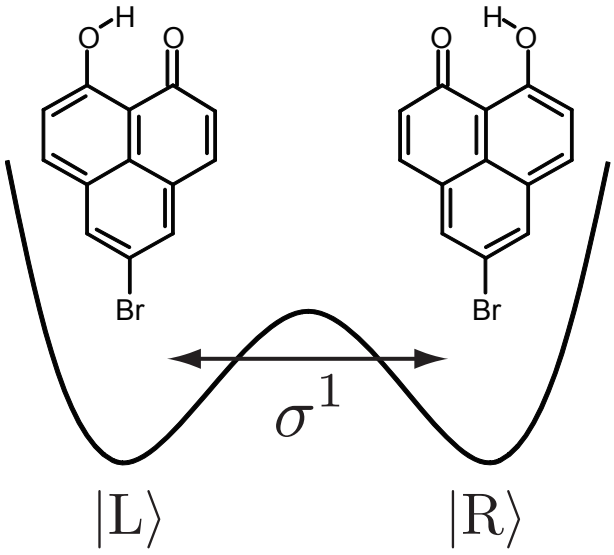

Figure 1: Schematic diagram of intramolecular proton transfer in the BHP molecule.

calculations with plane-wave basis sets can be useful (*e.g.*, see Figure 4 in Ref. [27]). Nevertheless, there is still a gap in the discussion for understanding the ferroelectric properties between studies of local molecular interactions and long-range interactions that cause dielectric ordering.

These considerations led us to propose a novel computational scheme that combines fragment molecular orbital (FMO) calculations with Monte Carlo (MC) simulations, in which the former introduces to the latter electronic polarization effects induced by the various proton configurations of surrounding molecules. In its application to the BHP crystal, we discovered the importance of $\mathrm{C}-\mathrm{H}\cdots\mathrm{O}$ type intermolecular weak hydrogen bonding, through which the relative configurations of adjacent intramolecular hydrogen bonds strongly affect dipole induction [27, 28]. This conflicts with the prevailing presumption that BHP molecules are relatively isolated in the crystal [16, 19]. We have previously demonstrated that dipole induction correction almost doubles the calculated phase transition temperature of the BDP crystal and gives better agreement with experiments [27]. However, this study did not explicitly take account of proton tunneling, which is an appropriate assumption for BDP but not for BHP. Therefore, in this work we extend the method to path integral MC (PIMC) method, which is one of the quantum MC methods [29], to account for proton tunneling, and study

the isotope effect on the dielectric phase transition behavior.

In the study of order–disorder type hydrogen-bonded ferroelectrics, the transverse Ising model has often been successfully used to reproduce the isotope effect [30–32]. By ignoring higher vibrational states in the relevant temperature range, the problem is reduced to a two-level system with tunneling between two degenerate localized states [33] [1]. In this paper, the transverse tunneling Hamiltonian is combined with our correction scheme for dipole induction. We thus constructed the effective classical Hamiltonian via the Suzuki–Trotter decomposition [34–36], and performed PIMC simulations to calculate the temperature-dependence of the dielectric constant for homogeneous crystals with different values of the tunneling energy corresponding to BHP, BDP, and their isotope mixtures.

The paper is organized as follows. In Section 2, we describe the Hamiltonian involving the tunneling effect and map it to an effective classical Hamiltonian for the MC simulations using the Suzuki–Trotter formula. Sections 3 and 4 present computational details and the simulation results. The last section gives the conclusions of the study. Some technical details of the new PIMC method are given in the Appendix.

2. Dipole–Dipole Interaction Hamiltonian with Tunneling Effect

We constructed the dipolar model system of the BHP molecular crystal in a same manner as a previous study [27]. That is, using the crystal structure data in Ref. [23], and positioning the molecular electric dipole moment $\mathbf{p} = (p_x, p_y, p_z)$ at the center of mass of each molecule in a Cartesian coordinate system in which the $x(y)$-axis coincides with the crystallographic $a(b)$-axis. In Figure 2, we show the schematic structure of the BHP crystal. We define the transverse and longitudinal dipole moments ($p_\perp$ and $p_\parallel$, respectively) by $p_\perp = \sqrt{p_x^2 + p_z^2}$ and $p_\parallel = p_y$. The transverse dipole moment is inverted by proton transfer.

[1] The frequency of the typical O–H stretching mode is approximately 3000 cm^{-1}($\sim$4300 K). As shown in the case of the square-well potential, the eigenenergy in the potential is inversely proportional to the square of the width. Hydrogen bonding extends the range of motion of the hydrogen atom by almost twice. Therefore, there should be a gap of $\sim$1000 K between the tunneling-split states and the vibrational excited state.

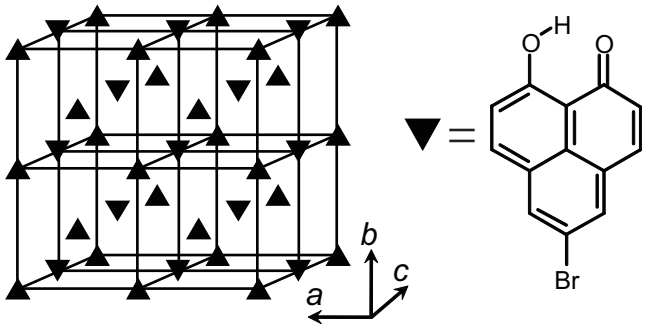

Figure 2: Schematic structure of the BHP crystal. Each triangle represents a BHP molecule and each inverted triangle represents an inverted BHP molecule. The arrangement of the molecules is based on the crystal structure data in Ref. [23].

Taking into account the tunneling effect, the Hamiltonian is expressed as

$$\begin{aligned}\mathcal{H} = &-\sum_{j=1}^{N} \Omega_j \sigma_j^1 \\ &+ \frac{1}{4\pi\varepsilon_0} \sum_{j<k} \frac{1}{r_{jk}^3} \left[\mathbf{p}_j \cdot \mathbf{p}_k - \frac{3(\mathbf{p}_j \cdot \mathbf{r}_{jk})(\mathbf{p}_k \cdot \mathbf{r}_{jk})}{r_{jk}^2} \right],\end{aligned} \tag{1}$$

with the dipole moment at site j described by

$$\mathbf{p}_j = (\sigma_j^3 p_{jx}, p_{jy}, \sigma_j^3 p_{jz}), \tag{2}$$

where $\sigma_i^\alpha (\alpha = 1, 3)$ are the Pauli spin matrices $\sigma^1 = \begin{pmatrix} 0 & 1 \\ 1 & 0 \end{pmatrix}$ and $\sigma^3 = \begin{pmatrix} 1 & 0 \\ 0 & -1 \end{pmatrix}$, $\mathbf{r}_{jk}$ is the position vector from site j to k, ε_0 is the vacuum permittivity, Ω_j is the tunneling frequency at site j, and $r_{jk} = |\mathbf{r}_{jk}|$. In the following, we use L (or R) for the two localized states (see Figure 1). The states $|\mathrm{L}\rangle$ and $|\mathrm{R}\rangle$ are expressed as the eigenstate of the two-state system, $|\mathrm{L}\rangle = \begin{pmatrix} 1 \\ 0 \end{pmatrix}$ and $|\mathrm{R}\rangle = \begin{pmatrix} 0 \\ 1 \end{pmatrix}$, respectively. The operator σ^1 maps the state from $|\mathrm{L}\rangle$ to $|\mathrm{R}\rangle$ and *vice versa*, and its coefficient Ω_j provides the rate of tunneling from one state to the other. Thus, the first term of Eq. (1) describes the proton tunneling. In Eq. (1), each molecular site can have different tunneling frequency to describe the H/D-mixed crystal. In addition, the states

$|\mathrm{L}\rangle$ and $|\mathrm{R}\rangle$ are eigenstates of the operator σ^3 with eigenvalues $+1$ and -1, respectively. Therefore, Eq. (2) indicates that the transverse dipole moment of the BHP molecule is inverted by proton transfer.

We use the Suzuki–Trotter formula [34–36]

$$e^{A+B} = \lim_{M\to\infty} \left(e^{A/M} e^{B/M}\right)^M , \tag{3}$$

to evaluate the partition function of the quantum Hamiltonian (1): $Z = \mathrm{Tr}\left\{e^{-\beta\mathcal{H}}\right\}$, where β is the inverse temperature. We can follow almost the same procedure as the conventional transverse Ising Hamiltonian [32, 34, 37, 38], with a straightforward inclusion of our new dipole-correction scheme. Using the complete set of eigenvectors of the operator σ_j^3, we obtain

$$\begin{aligned} Z &= \lim_{M\to\infty} Z_M(\beta) && (4)\\ &= \lim_{M\to\infty} \sum_{\{\sigma\}} \left(\prod_{j=1}^{N} A_j\right)^M \\ &\quad \times \exp\left[\sum_{l=1}^{M}\left(-\frac{\beta J_l}{M} + \sum_{j=1}^{N} \gamma_j \sigma_{j,l}\sigma_{j,l+1}\right)\right], && (5) \end{aligned}$$

with

$$A_j = \left\{\frac{1}{2}\sinh\left(\frac{2\beta\Omega_j}{M}\right)\right\}^{1/2}, \tag{6}$$

$$\gamma_j = \frac{1}{2}\log\left[\coth\left(\frac{\beta\Omega_j}{M}\right)\right], \tag{7}$$

$$J_l = \frac{1}{4\pi\varepsilon_0}\sum_{j<k}\frac{1}{r_{jk}^3}\left[\mathbf{p}_j^{(l)}\cdot\mathbf{p}_k^{(l)} - \frac{3\left(\mathbf{p}_j^{(l)}\cdot\mathbf{r}_{jk}\right)\left(\mathbf{p}_k^{(l)}\cdot\mathbf{r}_{jk}\right)}{r_{jk}^2}\right], \tag{8}$$

and

$$\mathbf{p}_j^{(l)} = \left(\sigma_{j,l}p_{jx}, p_{jy}, \sigma_{j,l}p_{jz}\right), \tag{9}$$

where $\sigma_{j,l} = \pm 1$ are the eigenvalues of the σ^3 operator on site (j,l). The indices j and l indicate the site in the crystal and that in the additional (Trotter) dimension, respectively. We thus obtain the effective classical Hamilto-

nian in the Mth Trotter approximation as

$$\begin{aligned}\mathcal{H}_{\rm eff}(\beta) &= \sum_{l=1}^{M}\left(\frac{J_l}{M}-\sum_{j=1}^{N}\frac{\gamma_j}{\beta}\sigma_{j,l}\sigma_{j,l+1}\right)\\ &\quad -\frac{M}{2\beta}\sum_{j=1}^{N}\log\left\{\frac{1}{2}\sinh\left(\frac{2\beta\Omega_j}{M}\right)\right\}. \end{aligned} \tag{10}$$

The appearance of the Trotter dimension indicates that the Hamiltonian (Eq. (10)) represents a $(3+1)$-dimensional $(N \times M)$ classical system. This system is quite anisotropic: the interaction in the subsystem with each Trotter index l (Trotter slice) is the M-fold diluted dipole–dipole interaction J_l/M minus the nearest neighbor interaction with a strength of γ_j/β along the Trotter direction.

The last term of Eq. (10), which originates from the factor A_j in Eq. (5), has not been previously reported [32, 36–39]. This is because it does not depend on the spin configurations and it is canceled in the calculation of the expectation values of physical quantities. However, when we use the replica exchange MC method [40], this term is essential for the following reason. In the replica exchange MC method, a series of system replicas with different temperatures are simultaneously and independently simulated, during the course of which the configurations of replicas are exchanged. If the Metropolis method is used, as in this work, the acceptance probability for the replica exchange trial is given by

$$P_{\rm ex} = \min\left\{1, \exp\left[(\beta_k-\beta_{k+1})(\mathcal{H}_{\rm eff}(\beta_k)-\mathcal{H}_{\rm eff}(\beta_{k+1}))\right]\right\}. \tag{11}$$

Indeed, the effective Hamiltonians with two neighboring temperatures are generally involved in the replica exchange simulations irrespective of the sampling algorithm. Therefore, the last term in Eq. (10) cannot be omitted. Actually, this term was found to significantly contribute to the replica exchange process (see Appendix).

3. Computational Details

3.1. Evaluation of the Correction Factor

Prior to the MC simulations, we evaluated the correction factors for the molecular dipole moments. The method is identical to that in Ref. [27]. The

correction factors are defined as the relative changes of the dipole moment of the central molecules in trimers, and they were constructed for every relative position of the surrounding molecules in the crystal. Thus, the correction factors for transverse ($\Delta p_\perp$) and longitudinal ($\Delta p_\parallel$) components are expressed as

$$\Delta p_\perp = \frac{p_\perp^{\mathrm{tri}}}{p_\perp^{\mathrm{mon}}} - 1 \tag{12}$$

and

$$\Delta p_\parallel = \frac{p_\parallel^{\mathrm{tri}}}{p_\parallel^{\mathrm{mon}}} - 1, \tag{13}$$

respectively. The superscript "mon" indicates the dipole moment of an isolated monomer and "tri" indicates that of the central molecule in each trimer.

The dipole moment of the central molecule in the trimers is evaluated using the FMO-2 method [41], in which each monomer is treated as a fragment. As we have previously demonstrated, the induced dipole moment is sensitive to the intermolecular interactions of the trimer and the relative configurations of the intramolecular hydrogen bonds because of the differences in the electrophilicity of carbonyl and enolic oxygen atoms [27, 28].

We considered all 14 possible trimer configurations in the BHP crystal structure, which are labeled A to N according to their relative position in the crystal. The positional relations of the trimers are listed in Table 1 (also see Supporting Information for the structures of the trimers and their positions). For each trimer, calculations were performed for all hydrogen transfer positions in the two surrounding molecules (the configurations are denoted hereafter as LL, LR, RL, and RR) with the hydrogen atom of the central molecule in state L (which is sufficient because of the crystal symmetry).

The calculations of the dipole correction factors of Eqs. (12) and (13) were performed using the GAMESS program package [42]. Since the correction factors are the effects of dipole induction in the molecular crystal, the long-range intermolecular interaction may be significant. To effectively take into account electron correlation and long-range interactions, we used the LC-BOP (long-range-corrected Becke 1988 exchange functional with one-parameter progressive correlation) functional with the range-separation parameter $\mu = 0.33$ [43]. The basis set was cc-pVDZ for all atoms. We also performed calculations at the MP2/cc-pVDZ level. The dipole moments of the BHP monomer at these two levels of theory as well as at the restricted Hartree–Fock (RHF) level with the 6-31G(d,p) basis set are listed in Table 2.

Table 1: List of the trimers for the evaluation of correction factors[a]

Trimer	Position[b]			Trimer	Position[b]		
	X	Y	Z		X	Y	Z
A	± 1.0	0.0	0.0	H	± 0.5	-0.5	± 0.5
B	0.0	± 1.0	0.0	I	± 0.5	0.5	± 0.5
C	0.0	-1.0	± 0.5	J	± 0.5	-0.5	∓ 0.5
D	0.0	1.0	± 0.5	K	± 0.5	0.5	∓ 0.5
E	0.0	0.0	± 1.0	L	0.0	0.0	± 0.5
F	± 0.5	-0.5	0.0	M	± 1.0	0.0	± 0.5
G	± 0.5	0.5	0.0	N	± 1.0	0.0	∓ 0.5

[a] This table is reproduced from Table 1 in Ref. [27]. [b] The relative positions of the molecular centers of the molecules that form trimers with a reference (0, 0, 0) molecule are shown. The H atom in the intramolecular hydrogen bond of the reference molecule is arranged on the upper side in the longitudinal direction ($+b$). The positions X, Y, and Z are in units of the lattice parameters a, b, and c, respectively (the double sign applies in the same order).

The dipole moment significantly decreased by including electron correlation (also see Table 4 in Ref. [27]). The dipole correction factors for the LC-BOP functional and the MP2 level of theory will be compared in Section 4.1.

3.2. Path Integral Monte Carlo Simulations

Because the procedure for the classical MC case is described in Ref. [27], we will only outline the features introduced in the present PIMC simulations.

The program for the PIMC simulations was developed by one of the authors. In the MC simulations, we defined the MC unit cell to be two crystallographic unit cells along the a- and b-axis and one crystallographic unit cell along the c-axis (see Figure 3 in Ref. [27]). The number of dipoles in real space N was $16N_aN_bN_c$, where N_a, N_b, and N_c are the number of MC unit cells along the a-, b-, and c-direction, respectively. As described in Section 2, we introduced one additional dimension along the Trotter axis in the PIMC simulations. Therefore, the total number of dipoles in the simulated system was $16MN_aN_bN_c$. Periodic boundary conditions were applied to the system.

We used the replica exchange MC method [40] with the effective Hamiltonian (Eq. (10)). As mentioned in Section 2, the system described with the effective Hamiltonian (Eq. (10)) is quite anisotropic in the Trotter direction.

Table 2: Dipole moment of the BHP monomer

Computational level	Dipole moment / D[a]		
	$\left\|p_{\perp}^{\mathrm{mon}}\right\|$	$\left\|p_{\parallel}^{\mathrm{mon}}\right\|$	$\left\|p^{\mathrm{mon}}\right\|$
LC-BOP/cc-pVDZ	0.585	2.015	2.098
RHF/6-31G(d,p)	0.742	2.928	3.020
MP2/cc-pVDZ	0.415	1.624	1.676

[a] 1 D = 3.336 $\times 10^{-30}$ C m.

Thus, the conventional single-spin-flip method is inappropriate for updating each replica. We used the spin-cluster-flip method in Ref. [44] to update each replica, in which M spins (dipoles) on the Trotter axis are treated as a cluster. The index of the cluster in real space is selected randomly and the next state of the cluster is determined from all possible 2^M states of the cluster by the heat bath method [45]. The probability with which we choose state ν ($\nu = 1, 2, \cdots, 2^M$) is written as

$$w_\nu = \frac{e^{-\beta \mathcal{H}_{\mathrm{eff}}^{(\nu)}}}{\sum_{\mu=1}^{2^M} e^{-\beta \mathcal{H}_{\mathrm{eff}}^{(\mu)}}}, \tag{14}$$

where $\mathcal{H}_{\mathrm{eff}}^{(\mu)}$ is the effective Hamiltonian of the cluster in state μ. We define 1 MC step as N trials of the cluster flip (*i.e.*, each cluster is selected once on the average).

The number of replicas for the exchange MC method was 96, and these replicas were distributed in the temperature ranges 5–55 K for BHP and 5–70 K for BDP and the mixtures. The temperature intervals of the replicas were set so that the inverse temperature points $\{\beta_k\}$ would be distributed at uniform intervals (see Appendix). The initial configurations of the replicas were randomly selected and all replicas were thermalized without replica-exchange. After the thermalization, data were collected for analysis. We performed 10 000 MC steps for the thermalization and 100 000 MC steps for the sampling. The replica-exchange trial during the sampling process was made every 5 MC steps with the probability defined by Eq. (11). The system size (in real space) investigated here was $(N_a, N_b, N_c) = (3, 3, 6)$, which corresponds to $N = 864$ dipoles, and the number of Trotter slices M was from 2 to 12 to extrapolate to $M \to \infty$. The cutoff radius for the

dipole–dipole interaction was set to 20 Å, which is the same as that used in a previous study [27].

The dipole moments were corrected every MC step using the results described in Section 4.1. For every site j, we compose the trimers in Table 1 so that site j is the central molecule of each trimer. According to the configurations of the hydrogen atoms of the surrounding molecules (LL, LR, RL, or RR), the correction factor is applied to the dipole moment. We define the corrected dipole moment of site j as

$$p_{j\mu} = \left(1 + \sum_{\text{trimer}} \Delta p_\mu\right) p_\mu^{\text{mon}} \qquad (\mu = \perp, \parallel). \tag{15}$$

Although we applied the correction factors of all 14 directions of the interaction for the transverse component, the correction factors for the longitudinal component were not taken into account because the latter is almost independent of the relative configurations of the hydrogen atoms (see Section 4.1).

4. Results and Discussion

4.1. Relative Changes of the Dipole Moment

Figure 3 shows the relative changes of the transverse and longitudinal dipole moments obtained from the FMO calculation. In addition to the LC-BOP/cc-pVDZ and MP2/cc-pVDZ results, we also plot the previous results with RHF/6-31G(d,p) as a reference [27]. In this figure, the horizontal axis represents the labels of the trimers (see Table 1 and Supporting Information) and the vertical axis represents the relative changes of the transverse (Figure 3(a)) and longitudinal (Figure 3(b)) components of the dipole moment defined by Eqs. (12) and (13).

It has been found that the transverse component is mainly affected from three directions [27]: F, I, and L in Figure 3(a). With regard to trimers F and I, we reported the existence of intermolecular $\mathrm{C-H\cdots O}$ hydrogen bonding from the geometric features, natural population analysis, and Atoms-in-Molecules analysis [27, 28]. The large variation of the transverse component is because of the difference in the electrophilicity of the carbonyl and enolic oxygen atoms of surrounding molecules involved in the intermolecular hydrogen bonding. The difference causes the bias in the atomic charge of the central molecule of the trimer, which results in dipole induction. In the

case of trimer L, π–π stacking interactions are involved. We suggest that the change of the electronic structure between the molecular planes by proton transfer causes the variation of the transverse component. However, the longitudinal component in Figure 3(b) is insensitive to changes of the relative configurations of hydrogen atoms. This result is reasonable because this direction is perpendicular to that of proton transfer [27, 28].

Compared with the results obtained using RHF/6-31G(d,p), the range of changes using LC-BOP/cc-pVDZ is slightly larger. However, as shown in Table 2, the absolute dipole moment calculated using LC-BOP/cc-pVDZ is smaller than that calculated with RHF/6-31G(d,p). Thus, it is suggested that the dipole moment in the crystal calculated using LC-BOP/cc-pVDZ will also be smaller than that calculated using RHF/6-31G(d,p).

From Figure 3(a), the transverse component calculated using MP2/cc-pVDZ shows a large variation. This is because of the definition of the relative change (Eq. (12)). As shown in Table 2, the dipole moment of the isolated monomer $p_{\perp}^{\mathrm{mon}}$, which appears in the denominator in Eq. (12), calculated with MP2/cc-pVDZ is smaller than that calculated using the other methods. Therefore, relative changes are emphasized in Figure 3. The relationship between the dipole moment and the relative changes is further discussed in Section 4.4 in conjunction with the dielectric phase transition temperature.

4.2. Pure BHP Crystal

Here, we describe the PIMC simulation of the pure BHP crystal. In Sections 4.2 and 4.3, we focus on the results obtained using LC-BOP/cc-pVDZ. The qualitative discussion also applies to the results using MP2/cc-pVDZ. The quantitative differences will be mentioned in Section 4.4.

The values of Ω_j were set to the experimentally determined value of $\Omega_{\mathrm{H}} = 60$ K for all j [22]. The temperature range was set from 5 to 55 K. In Figure 4, we plot the static dielectric constant $\varepsilon = 1 + \chi$ as a function of temperature T, where the susceptibility χ is calculated from the fluctuation of the x components of polarization, which corresponds to the experimentally measured direction[16, 17]:

$$\chi = \frac{4\left(\langle(\sum_j p_{jx})^2\rangle - \langle\sum_j p_{jx}\rangle^2\right)}{NV\varepsilon_0 k_{\mathrm{B}} T}, \tag{16}$$

where k_{B} is the Boltzmann constant, V is the volume of the unit cell, and the brackets $\langle\ \rangle$ denote the MC average.

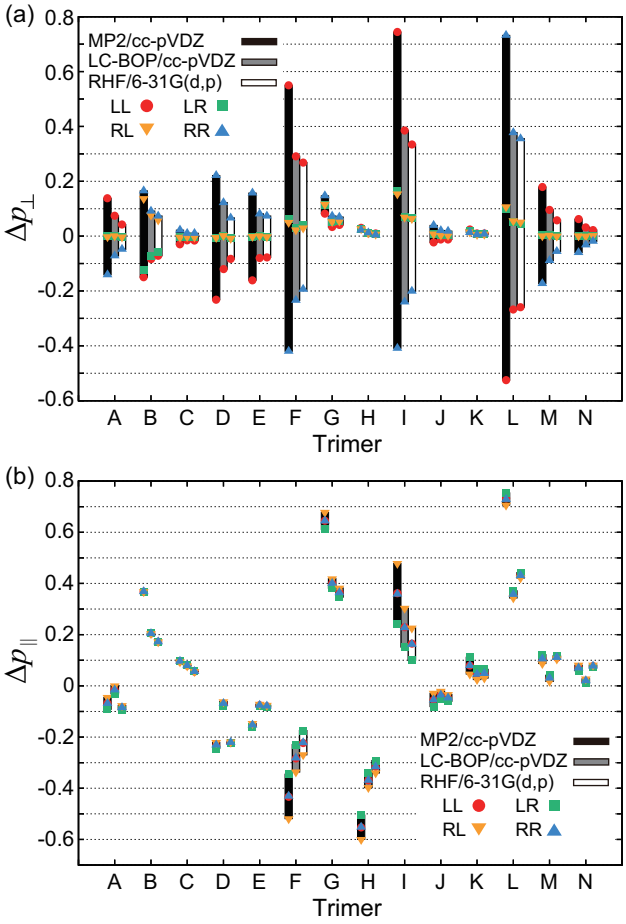

Figure 3: Relative change of (a) the transverse and (b) the longitudinal component of the dipole moment. In each type of trimer, four values corresponding to the combination of the configurations of the hydrogen atoms of the surrounding molecules (LL, LR, RL, and RR) are plotted. The bars represent the range between the maximum and minimum values for each type of trimer. For the labels on the horizontal axis, see the Supporting Information.

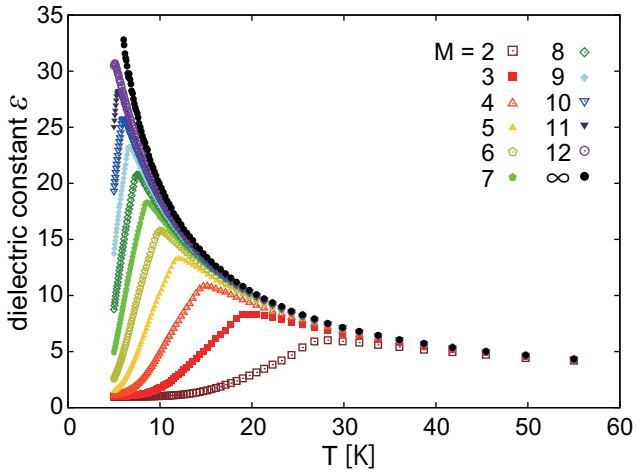

Figure 4: Plot of the dielectric constant $\varepsilon = 1 + \chi$ with $\Omega_j = 60$ K for all j (BHP crystal) against temperature T. The symbol ∞ (solid black circles) indicates the points obtained by extrapolation according to Eq. (17).

The dielectric constant for the quantum system was evaluated by extrapolating the data at each temperature to the limit $M \to \infty$ using the well-known convergence relationship

$$A(M) = A_\infty + \frac{A_2}{M^2} + O\left(\frac{1}{M^4}\right), \tag{17}$$

where $A(M)$ is the average of any quantum operator A taken with respect to the effective Hamiltonian in the Mth Trotter approximation [35, 46]. This relationship also holds for the operators affected by the dipole correction, because the correction factors are determined uniquely for every state in the system and thus the "dipole-corrected" operators are unique.

We found that fitting to Eq. (17) only applies for data points above the temperature of the peak of each M, and these data points are thus used for the extrapolation. The extrapolated points are shown in Figure 4 (black filled circles). Figure 4 shows that the extrapolated dielectric constant monotonically increases as the temperature decreases. A peak of dielectric constant corresponds to a phase transition, and thus our result indicates that phase transition is not observed down to ~ 6 K.

To evaluate the phase transition temperature in BHP crystal, we investigated the relationship between the temperature at the peak and the number of Trotter slices M. Figure 5 shows the plot of the temperature at the peak

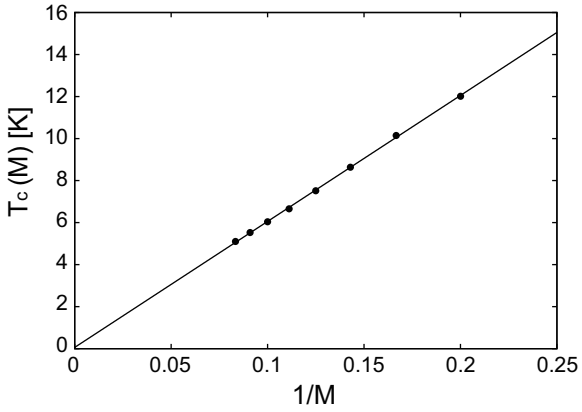

Figure 5: Relationship between the temperature at the peak of the dielectric constant $T_{\rm c}(M)$ and the number of Trotter slices $1/M$ in the case of the BHP crystal ($\Omega_j = 60$ K for all j). The data from $M = 5$ to 12 were used because the data with the smaller M are less relevant and subject to larger error in reading the peak position.

for each M in Figure 4, $T_{\rm c}(M)$, as a function of $1/M$. It is reasonable that the temperature at the peak is inversely proportional to M, because, as mentioned in Section 2, the interaction in real space is M-fold diluted. Then, we fitted the data to the function:

$$T_{\rm c}(M) = \frac{p}{M} + T_{\rm c}(\infty), \tag{18}$$

and found that $p = 60.0 \pm 0.5$ K and $T_{\rm c}(\infty) = 0.1 \pm 0.6$ K, which includes the error due to the discrete temperature interval of the data in Figure 4. The value of $T_{\rm c}(\infty)$ corresponds to the estimated peak temperature in the full quantum system ($M \to \infty$) and it indicates that the phase transition does not occur down to ~ 1 K, which is in agreement with the experimental results. However, the calculated absolute value of ε in the low temperature region overestimates the experimental value [17]. One possible reason for this could be that the experimental result is the dynamic dielectric constant measured by applying an AC electric field, which may suppress the quantum fluctuations, while our result is the static dielectric constant.

4.3. Pure BDP Crystal

Next, we simulated the case of the pure BDP crystal. The values of Ω_j were set to $\Omega_{\rm D} = 10$ K for all j, which has been estimated from the spectroscopically measured ratio $\Omega_{\rm H}/\Omega_{\rm D}$ of the mother compound 9-hydroxyphenalenone [47]. The temperature range was set from 5 to 70 K.

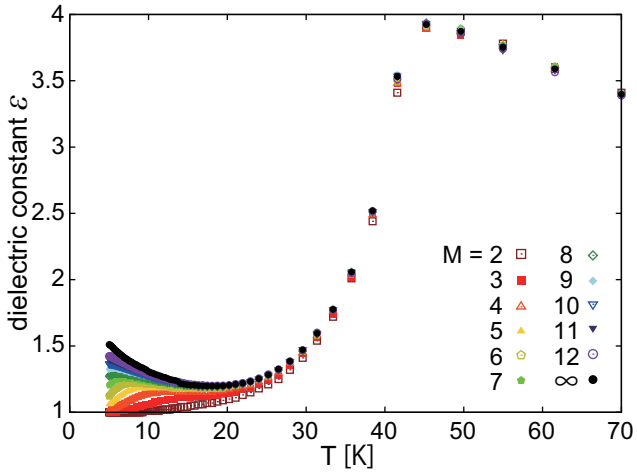

Figure 6: Plot of the dielectric constant $\varepsilon = 1 + \chi$ with $\Omega_j = 10$ K for all j (BDP crystal) against temperature T. The symbol ∞ (black solid circles) indicates the points obtained by extrapolation according to Eq. (17).

Figure 6 shows the temperature dependence of the dielectric constant for each M. One common peak is observed at approximately 45 K for all M, which corresponds to the phase transition temperature T_c. This transition temperature is slightly lower than the value of 50 K reported in a previous study calculated with correction factors at the RHF level [27], and it is in better agreement with the experimental value of 37 K.

In the temperature region above 30 K, the values of ε from different M agree well. In the low-temperature region, however, the dielectric constant gradually increases with increasing M. The extrapolated plot in this region shows that the dielectric constant increases with decreasing temperature. This behavior is not directly related to the experimentally measured peak around 20 K that is considered to originate from the incommensurate-commensurate phase transition [17]. We rather attribute this behavior to quantum fluctuations because of the tunneling term, whose strength Ω_D is comparable to this temperature region. We will further discuss this point in the following section.

4.4. Crystals with Intermediate Values of Ω_H *and* Ω_D

Finally, we also investigated the case of homogeneous crystals with intermediate values of Ω, assuming the case of the BHP/BDP-mixed crystal. To relate the tunneling frequency and the H/D ratio in the system, we define

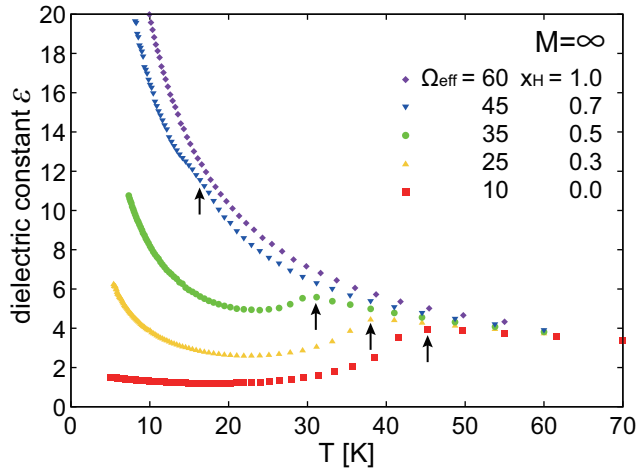

Figure 7: Dielectric constant extrapolated along the Trotter direction. The triangles, circles, and inverted triangles are the results of the uniform systems with $\Omega_{\rm eff} = 25$, 35, and 45 K, respectively. The results of BHP ($\Omega_{\rm eff} = \Omega_{\rm H} = 60$ K) and BDP ($\Omega_{\rm eff} = \Omega_{\rm D} = 10$ K) are also plotted. The arrows indicate the phase transition temperatures defined as the inflection point of the ε–T curve. The terms up to the fourth order in Eq. (17) were used for the extrapolation.

the effective tunneling frequency $\Omega_{\rm eff}$ as

$$\Omega_{\rm eff} = x_{\rm H}\Omega_{\rm H} + (1 - x_{\rm H})\Omega_{\rm D}, \tag{19}$$

where $x_{\rm H}$ is the proton concentration ratio (*i.e.*, H:D = $x_{\rm H} : 1 - x_{\rm H}$).

In Figure 7, we show the calculated dielectric constants for $\Omega_{\rm eff} = 10$ ($x_{\rm H} = 0.0$, pure BDP), 25 ($x_{\rm H} = 0.3$), 35 ($x_{\rm H} = 0.5$), 45 ($x_{\rm H} = 0.7$), and 60 K ($x_{\rm H} = 1.0$, pure BHP). As $\Omega_{\rm eff}$ increases, the temperature at the peak decreases from ~ 45 K in the BDP crystal with $\Omega_{\rm eff} = 10$ K to there being no peak (or bending) at $\Omega_{\rm eff} = 60$ K. From these results, we redefine the phase transition temperature $T_{\rm c}$ as the inflection point of the ε–T curve, which is shown by the arrows in Figure 7.

We qualitatively explain the Ω-dependence of the phase transition temperature seen in Figure 7 using the mean field theory (MFT) of the transverse Ising model, which has previously been applied to an inorganic H/D-mixed system [48, 49]. In MFT, the phase transition temperature is given by

$$\frac{1}{|J|} = \frac{x_{\rm H}}{\Omega_{\rm H}} \tanh\left(\frac{\Omega_{\rm H}}{k_{\rm B}T_{\rm c}}\right) + \frac{1 - x_{\rm H}}{\Omega_{\rm D}} \tanh\left(\frac{\Omega_{\rm D}}{k_{\rm B}T_{\rm c}}\right), \tag{20}$$

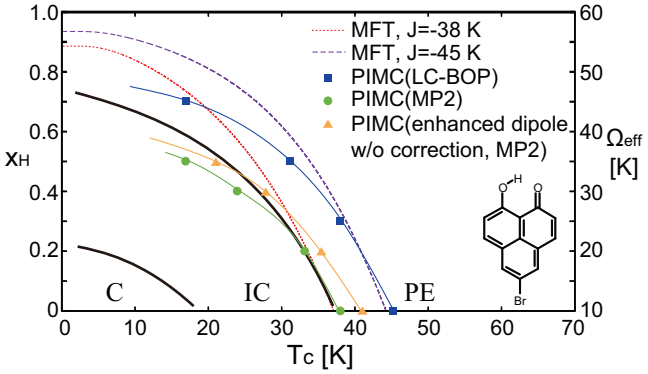

Figure 8: Phase diagram obtained from the PIMC simulations (blue, green, and yellow filled symbols), and the numerical calculations based on the MFT of the transverse Ising model (red dotted and purple dashed lines), which are compared with the experimental results (black solid lines). The blue, green, and yellow solid lines are merely guides to the eye. PE, IC, and C represent paraelectric, incommensurate, and commensurate, respectively. The parameter values used in the MFT calculations were $\Omega_{\rm H} = 60$ K, $\Omega_{\rm D} = 10$ K, and $J = -38$ or -45 K. The effective tunneling frequency $\Omega_{\rm eff}$ is defined in Eq. (19). The experimental data are taken from Ref. [51].

where J is the molecular field parameter defined by $\sum_j J_{ij}$ [50]. In a previous study, we found that the molecular field parameter J was the same order of magnitude as the phase transition temperature obtained using classical MC simulations [27]. Therefore, we estimate J to be approximately -45 K from the result of the BDP crystal (see Figure 6). Using the parameter values J, $\Omega_{\rm H}$, $\Omega_{\rm D}$, and $x_{\rm H}$, we numerically solved Eq. (20) for $T_{\rm c}$.

Figure 8 shows the resultant phase diagram along with experimental results (black solid lines) [51]. The results of the PIMC simulations using both LC-BOP/cc-pVDZ and MP2/cc-pVDZ are also plotted. Here, we compare the results of our calculations with the experimental paraelectric (PE)–incommensurate (IC) phase transition temperature, which reflects the typical strength of the intermolecular interactions in the crystal. In the result of the MFT calculation with $J = -45$ K (purple dashed line), $T_{\rm c} \sim 45$ K at $x_{\rm H} = 0$ ($\Omega_{\rm eff} = \Omega_{\rm D}$), which corresponds to the BDP crystal. Moreover, the results show that no phase transition occurred at $x_{\rm H} = 1$ ($\Omega_{\rm eff} = \Omega_{\rm H}$), which corresponds to the BHP crystal. This is consistent with the results obtained from the PIMC simulations. However, there is a discrepancy between the results of PIMC and MFT in the intermediate region of $x_{\rm H}$. Furthermore, in MFT, even if we adjust J so that $T_{\rm c}$ at $x_{\rm H} = 0$ coincides with the experimental

value ($J = -38$ K, red dotted line), we could not describe the curvature of the x_{H}–T_{c} curve. In contrast, the curvature of the results of the PIMC simulations (blue and green solid lines) is similar to the experimental results (black solid lines).

It is noteworthy that our result using PIMC with MP2/cc-pVDZ is quantitatively consistent with the experimental result, especially in the small x_{H} region. The resultant critical temperature is 39 K at $x_{\mathrm{H}} = 0$, while the experimental value is 37 K. The values of the enhanced transverse dipole moment in the AFE phase are 0.893 (LC-BOP/cc-pVDZ) and 0.854 D (MP2/cc-pVDZ). In a previous paper, we reported that the value with a lower computational level (RHF) was 0.98 D [27]. Although all of the values are approximately 0.9 D, the components of the dipole moment are different. At the low computational level, the transverse dipole moment of the monomer $p_{\perp}^{\mathrm{mon}}$ is relatively large, but the correction factors are small. In contrast, at the high computational level, $p_{\perp}^{\mathrm{mon}}$ is relatively small, but the correction factors are large (see Table 2 and Figure 3). Using MP2/cc-pVDZ, the dipole moment increased by $0.854/0.415 = 2.06$ times as compared with that of the isolated molecule, which indicates a strong influence of weak intermolecular hydrogen bonding in the organic molecular crystals. In the intermediate region of x_{H}, however, our PIMC simulation underestimates the transition temperature. In our calculation, we evaluated the dipole moment and the correction factors with one fixed crystal structure (neutron diffraction data at 10 K [23]), and these parameter values were used in the PIMC simulations. However, the actual molecular conformations and crystal structures may depend on the temperature. Proper modeling of the softness of the molecular crystal may also affect the results, although the effect would be rather subtle such that the direction of change is not trivial.

To gain further insight into the curvature of the phase diagram, we also performed PIMC simulations without the dipole correction but with a transverse dipole moment of 0.854 D in the AFE phase at the MP2/cc-pVDZ level. The result is shown by the yellow triangles and solid line in Figure 8. The curvature of the x_{H}–T_{c} curve is almost the same as the other PIMC results. Therefore, we conclude that the good agreement of the curvature of the PIMC results with experiment is due to the inclusion of long-range interactions.

5. Concluding Remarks

We have investigated the tunneling effect on the dielectric properties of the hydrogen-bonded material BHP by extending our MC method with FMO-derived dipole corrections to the PIMC method. In the case of the pure BHP crystal, the results show that the phase transition does not occur down to ~ 1 K, which is consistent with experiment, as the phase transition is suppressed by quantum fluctuations due to the tunneling effect of the hydrogen atoms. In contrast, in the case of the pure BDP crystal, the phase transition occurs at approximately 45 K, and the transition temperature is not affected by tunneling. This is also consistent with the experimental results.

Another improvement from the previously reported method is the reevaluation of the dipole correction parameters at higher computational levels of theory. This resulted in a greater influence of intermolecular hydrogen bonding and better agreement of the phase transition temperature with experiment.

We also simulated homogeneous crystals with intermediate values of Ω assuming average values according to the composition of the BHP/BDP mixture. As a result, the phase diagram of the transition temperature $T_{\rm c}$ versus the mixing ratio agreed with experimental curve.

Although this work used the effective tunneling frequency for the isotope mixture, our Hamiltonian (Eq. (1)) can actually describe a microscopic mixture with different Ω_j values for every site j. Therefore, at the cost of calculating a sufficient number of statistical samples, we will be able to obtain the relationship between the microscopic domain structure (the distribution of H- and D-compounds) in the crystal and quantum fluctuations. To proceed in this direction, improvements in computational efficiency are required. In particular, the bottleneck of the calculation is the spin-cluster-flip algorithm, whose computational cost exponentially increases as 2^M and sufficiently large M is required for extrapolation to $M \to \infty$. Use of alternative cluster-flip methods, such as those that take the $M \to \infty$ limit prior to the simulation [52], and $O(N)$ algorithms [53] for the long-range interactions may be helpful. Works in these directions are currently underway and will be reported in due course.

Conflict of interest

The authors declare no conflict of interest.

Acknowledgements

We acknowledge the support by the Global COE Program "International Center for Integrated Research and Advanced Education in Materials Science" of the Ministry of Education, Culture, Sports, Science and Technology (MEXT) of Japan. HO is supported by the Special Postdoctoral Researchers Program at RIKEN. KA acknowledges support from KAKENHI Nos. 20108017 ("π-space") and 22550012. Numerical calculations were mainly performed using the RIKEN Integrated Cluster of Clusters (RICC) facility.

Appendix A. Effect of the Last Term in Effective Hamiltonian on the Replica Exchange Process

In the appendix, we discuss the contribution of the last term of the effective Hamiltonian (Eq. (10)) to the replica-exchange process. Let us write Eq. (10) as

$$\mathcal{H}_{\rm eff}(\beta) = F(\beta) + G(\beta), \tag{A.1}$$

where

$$F(\beta) = \sum_{l=1}^{M} \left(\frac{J_l}{M} - \sum_{j=1}^{N} \frac{\gamma_j}{\beta} \sigma_{j,l}\sigma_{j,l+1} \right), \tag{A.2}$$

and

$$G(\beta) = -\frac{M}{2\beta} \sum_{j=1}^{N} \log \left\{ \frac{1}{2} \sinh \left(\frac{2\beta\Omega_j}{M} \right) \right\}. \tag{A.3}$$

Then, the calculated value for the acceptance probability (Eq. (11)) is given by

$$\begin{aligned} &\exp\left[(\beta_k - \beta_{k+1})\Delta F(\beta_k, \beta_{k+1})\right] \\ &\quad \times \exp\left[(\beta_k - \beta_{k+1})\Delta G(\beta_k, \beta_{k+1})\right], \end{aligned} \tag{A.4}$$

where

$$\Delta F(\beta_k, \beta_{k+1}) = F(\beta_k) - F(\beta_{k+1}), \tag{A.5}$$

and

$$\Delta G(\beta_k, \beta_{k+1}) = G(\beta_k) - G(\beta_{k+1}). \tag{A.6}$$

By setting that $\Delta\beta = \beta_k - \beta_{k+1}$ (or $\Delta T = T_{k+1} - T_k$, where $k_{\rm B}T_k = 1/\beta_k$ and we take $\beta_k > \beta_{k+1}$ for convenience) is equal for all k, we can plot Eq. (A.4)

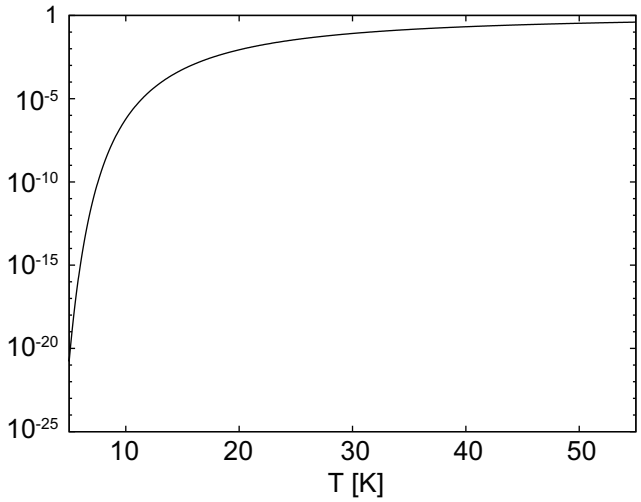

Figure A.9: Plot of the second factor of Eq. (A.4) with $\Delta T = 0.52$, $\Omega_j = 60$ for all j, $N = 864$, and $M = 8$.

as a function of temperature. We found that the second factor in Eq. (A.4) is $\sim 10^7$ times smaller than the first factor and determines the behavior in the low-temperature region for our system in the case of constant ΔT. In Figures A.9 and A.10, we plot the second factor of Eq. (A.4) for constant ΔT and $\Delta\beta$, respectively. The Trotter number was set to 8, and the conditions for the other parameters were chosen to be to the same as those used in the PIMC simulation of the pure BHP crystal (see Sections 3.2 and 4.2). Figure A.9 shows that, in the case of constant ΔT, the factor is extremely small in the low temperature region, where almost all trials for replica exchange will be rejected. This problem is less significant in the case of constant $\Delta\beta$ where the factor increases up to $\sim 10^{-2}$ as the temperature is decreased (Figure A.10). Its decrease in the direction of increasing temperature does not cause a problem because thermally-induced configuration changes are sufficient in this temperature region without replica exchange.

The above result indicates that the temperature interval between neighboring replicas is very important for MC simulations of quantum systems with the replica exchange method, because of the appearance of the extra term (Eq. (A.3)). Hukushima proposed a way to determine temperature points $\{\beta_k\}$ with an iterative procedure from the initial temperature set based on the one criterion that the acceptance probability for the replica exchange trial is equal for every pair of replicas at neighboring temperatures

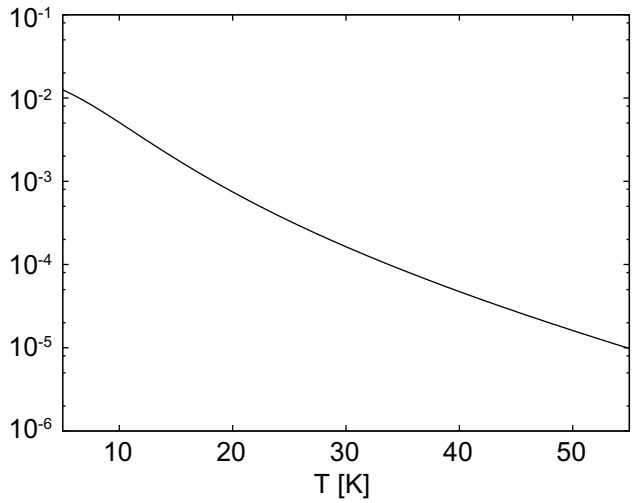

Figure A.10: Plot of the second factor of Eq. (A.4) with $\Delta\beta = 0.0019$, $\Omega_j = 60$ for all j, $N = 864$, and $M = 8$.

(see Appendix in Ref. [54]). However, it was found that when the initial temperature set has regular intervals of β, the temperature set reverts to the initial temperature set of $\{\beta_k\}$ after a few iteration steps, as long as the linear interpolation is used to evaluate $\mathcal{H}_{\rm eff}(\beta)$ at any temperature in the iteration process. In addition, when the initial temperature set has regular intervals of T, the temperature set approaches the equidistant distribution of β. Therefore, the equidistant set of β is an efficient choice for the replica exchange MC method.

Appendix B. Supplementary data

Supplementary data associated with this article can be found, in the online version, at

References

[1] A. Bussmann-Holder, N. Dalal, Order/disorder versus or with displacive dynamics in ferroelectric systems, in: N. Dalal, A. Bussmann-Holder (Eds.), Ferro- and Antiferroelectricity: Order/Disorder versus Displacive, Vol. 124, Springer-Verlag, Berlin Heidelberg, 2007, pp. 1–21.

[2] F. Jona, G. Shirane, Ferroelectric Crystals, Dover, New York, 1993.

[3] S. Horiuchi, Y. Tokura, Organic ferroelectrics, Nat. Mater. 7 (2008) 357–366.

[4] T. Akutagawa, H. Koshinaka, D. Sato, S. Takeda, S.-I. Noro, H. Takahashi, R. Kumai, Y. Tokura, T. Nakamura, Ferroelectricity and polarity control in solid-state flip-flop supramolecular rotators, Nat. Mater. 8 (2009) 342–347.

[5] S. Horiuchi, F. Ishii, R. Kumai, Y. Okimoto, H. Tachibana, N. Nagaosa, Y. Tokura, Ferroelectricity near room temperature in co-crystals of nonpolar organic molecules, Nat. Mater. 4 (2005) 163–166.

[6] S. Horiuchi, R. Kumai, Y. Tokunaga, Y. Tokura, Proton dynamics and room-temperature ferroelectricity in anilate salts with a proton sponge, J. Am. Chem. Soc. 130 (2008) 13382–13391.

[7] S. Horiuchi, Y. Tokunaga, G. Giovannetti, S. Picozzi, H. Itoh, R. Shimano, R. Kumai, Y. Tokura, Above-room-temperature ferroelectricity in a single-component molecular crystal, Nature 463 (2010) 789–792.

[8] K. Kobayashi, S. Horiuchi, R. Kumai, F. Kagawa, Y. Murakami, Y. Tokura, Electronic ferroelectricity in a molecular crystal with large polarization directing antiparallel to ionic displacement, Phys. Rev. Lett. 108 (2012) 237601.

[9] D.-W. Fu, H.-L. Cai, Y. Liu, Q. Ye, W. Zhang, Y. Zhang, X.-Y. Chen, G. Giovannetti, M. Capone, J. Li, R.-G. Xiong, Diisopropylammonium bromide is a high-temperature molecular ferroelectric crystal, Science 339 (2013) 425–428.

[10] S. Horiuchi, F. Kagawa, K. Hatahara, K. Kobayashi, R. Kumai, Y. Murakami, Y. Tokura, Above-room-temperature ferroelectricity and antiferroelectricity in benzimidazoles, Nat. Commun. 3 (2012) 1308.

[11] S. Horiuchi, R. Kumai, Y. Tokura, A supramolecular ferroelectric realized by collective proton transfer, Angew. Chem., Int. Ed. 46 (2007) 3497–3501.

[12] S. Horiuchi, R. Kumai, Y. Tokura, Hydrogen-bonded donor-acceptor compounds for organic ferroelectric materials, Chem. Commun. (2007) 2321–2329.

[13] S. Horiuchi, R. Kumai, J. Fujioka, Y. Tokura, Supramolecular approach to organic ferroelectrics, Physica B: Condensed Matter 405 (2010) S334–S337.

[14] S. Horiuchi, R. Kumai, Y. Tokura, Hydrogen-bonding molecular chains for high-temperature ferroelectricity, Adv. Mater. 23 (2011) 2098–2103.

[15] S. Horiuchi, R. Kumai, Y. Tokura, High-temperature and pressure-induced ferroelectricity in hydrogen-bonded supramolecular crystals of anilic acids and 2,3-di(2-pyridinyl)pyrazine, J. Am. Chem. Soc. 135 (2013) 4492–4500.

[16] T. Mochida, A. Izuoka, T. Sugawara, Y. Moritomo, Y. Tokura, Organic hydrogen-bonded dielectrics: Quantum paraelectricity based on tautomerization of 9-hydroxyphenalenone derivatives, J. Chem. Phys. 101 (1994) 7971–7974.

[17] Y. Moritomo, Y. Tokura, T. Mochida, A. Izuoka, T. Sugawara, Isotope effect on the dielectric phase transitions of 5-bromo-9-hydroxyphenalenone, J. Phys. Soc. Jpn. 64 (1995) 1892–1895.

[18] I. Tamura, Y. Noda, Y. Kuroiwa, T. Mochida, T. Sugawara, X-ray diffraction studies on the lock-in phase transition of intramolecular hydrogen-bonded compound d-BrHPLN, J. Phys.: Condens. Matter 12 (2000) 8345–8356.

[19] Y. Noda, I. Tamura, Y. Kuroiwa, T. Mochida, T. Sugawara, Incommensurate-commensurate phase transition of intramolecular hydrogen-bonded system: 5-bromo-9-deuteroxyphenalenone (d-BrHPLN), J. Phys. Soc. Jpn. 63 (1994) 4286–4289.

[20] T. Matsuo, K. Kohno, A. Inaba, T. Mochida, A. Izuoka, T. Sugawara, Calorimetric study of proton tunneling in solid 5-bromo-9-hydroxyphenalenone and deuteration-induced phase transitions in its deuteroxy analog, J. Chem. Phys. 108 (1998) 9809–9816.

[21] T. Matsuo, O. Yamamuro, A. Inaba, M. Ohama, T. Mochida, T. Sugawara, Far infrared spectra of tunneling protons in bromo-and iodo-hydroxyphenalenone at low temperature, Ferroelectrics 347 (2007) 101–110.

[22] T. Matsuo, K. Kohno, M. Ohama, T. Mochida, A. Izuoka, T. Sugawara, Infrared absorption by a tunneling proton in crystalline 5-bromo-9-hydroxyphenalenone, Europhys. Lett. 47 (1999) 36–41.

[23] R. Kiyanagi, H. Kimura, M. Watanabe, Y. Noda, T. Mochida, T. Sugawara, Indication of tunneling state of hydrogen atom in hydrogen-bonded material 5-bromo-9-hydroxyphenalenon studied by x-ray and neutron diffractions, J. Phys. Soc. Jpn. 77 (2008) 064602.

[24] C. Totsuji, Model analysis of isolated hydrogen bond, J. Phys. Soc. Jpn. 73 (2004) 1054–1058.

[25] S. P. Dolin, A. A. Khrulev, E. V. Polyakov, T. Y. Mikhailova, A. A. Levin, Low-temperature structural phase transitions in crystalline bromo and iodo 9-hydroxyphenalenone derivatives: Quantum chemistry employment, Int. J. Quantum Chem. 106 (2006) 2297–2304.

[26] S. P. Dolin, A. A. Levin, E. V. Polyakov, A. A. Khrulev, T. Y. Mikhailova, Hydrogen-bonded materials based on organic tautomeric molecules: Theoretical treatment, J. Mol. Struct. 790 (2006) 147–151.

[27] H. Otaki, K. Ando, The role of intermolecular hydrogen bond on dielectric properties in hydrogen-bonded material 5-bromo-9-hydroxyphenalenone: theoretical investigation, Phys. Chem. Chem. Phys. 13 (2011) 10719–10728.

[28] H. Otaki, K. Ando, Atoms-in-molecules analysis of the effect of intermolecular interactions on dielectric properties in hydrogen-bonded material 5-bromo-9-hydroxyphenalenone, Int. J. Quantum Chem. 113 (2013) 386–392.

[29] D. Chandler, Introduction to Modern Statistical Mechanics, Oxford University Press, New York, 1987.

[30] R. Blinc, B. Žekš, Dynamics of order-disorder-type ferroelectrics and anti-ferroelectrics, Adv. Phys. 21 (1972) 693–757.

[31] P. G. de Gennes, Collective motions of hydrogen bonds, Solid State Commun. 1 (1963) 132–137.

[32] B. K. Chakrabarti, A. Dutta, P. Sen, Quantum Ising Phases and Transitions in Transverse Ising Models, Springer-Verlag, Berlin, 1996.

[33] R. Blinc, B. Žekš, Soft Modes in Ferroelectrics and Antiferroelectrics, North-Holland Publishing Co., Amsterdam, 1974.

[34] M. Suzuki, Relationship between d-dimensional quantal spin systems and $(d+1)$-dimensional ising systems, Prog. Theor. Phys. 56 (1976) 1454–1469.

[35] M. Suzuki, Quantum statistical monte carlo methods and applications to spin systems, J. Stat. Phys. 43 (1986) 883–909.

[36] N. Hatano, M. Suzuki, Finding exponential product formulas of higher orders, Lect. Notes Phys. 679 (2005) 37–68.

[37] H. D. Raedt, A. Lagendijk, Monte carlo simulation of quantum statistical lattice models, Phys. Rep. 127 (1985) 233–307.

[38] B. K. Chakrabarti, A. Das, Transverse ising model, glass and quantum annealing, Lect. Notes Phys. 679 (2005) 3–36.

[39] A. Das, B. K. Chakrabarti, Colloquium: Quantum annealing and analog quantum computation, Rev. Mod. Phys. 80 (2008) 1061–1081.

[40] K. Hukushima, K. Nemoto, Exchange monte carlo method and application to spin glass simulations, J. Phys. Soc. Jpn. 65 (1996) 1604–1608.

[41] K. Kitaura, E. Ikeo, T. Asada, T. Nakano, M. Uebayasi, Fragment molecular orbital method: an approximate computational method for large molecules, Chem. Phys. Lett. 313 (1999) 701–706.

[42] M. W. Schmidt, K. K. Baldridge, J. A. Boatz, S. T. Elbert, M. S. Gordon, J. H. Jensen, S. Koseki, N. Matsunaga, K. A. Nguyen, S. Su, T. L. Windus, M. Dupuis, J. A. Montgomery, General atomic and molecular electronic structure system, J. Comput. Chem. 14 (1993) 1347–1363.

[43] H. Iikura, T. Tsuneda, T. Yanai, K. Hirao, A long-range correction scheme for generalized-gradient-approximation exchange functionals, J. Chem. Phys. 115 (2001) 3540–3544.

[44] O. Nagai, Y. Yamada, Y. Miyatake, Monte carlo simulations of three-dimensional heisenberg and transverse-ising magnets, in: M. Suzuki (Ed.), Quantum Monte Carlo Methods in Equilibrium and Nonequilibrium Systems, Springer-Verlag, Heidelberg, 1987, pp. 95–103.

[45] Y. Miyatake, M. Yamamoto, J. J. Kim, M. Toyonaga, O. Nagai, On the implementation of the 'heat bath' algorithms for monte carlo simulations of classical heisenberg spin systems, J. Phys. C: Solid State Phys. 19 (1986) 2539–2546.

[46] M. Suzuki, Transfer-matrix method and monte carlo simulation in quantum spin systems, Phys. Rev. B 31 (1985) 2957–2965.

[47] V. E. Bondybey, R. C. Haddon, J. H. English, Fluorescence and phosphorescence of 9-hydroxyphenalenone in solid neon and its hydrogen tunneling potential function, J. Chem. Phys. 80 (1984) 5432–5437.

[48] Y. Moritomo, Y. Tokura, N. Nagaosa, T. Suzuki, K. Kumagai, Quantum phase transition in $K_3D_{1-x}H_x(SO_4)_2$, Phys. Rev. Lett. 71 (1993) 2833–2836.

[49] Y. Moritomo, Y. Tokura, N. Nagaosa, T. Suzuki, K. Kumagai, Role of the proton tunneling in the phase transition of $K_3D_{1-x}H_x(SO_4)_2$, J. Low Temp. Phys. 99 (1995) 55–70.

[50] M. E. Lines, A. M. Glass, Principles and Applications of Ferroelectrics and Related Materials, Clarendon Press, Oxford, 1977.

[51] Y. Noda, I. Tamura, T. Hayashide, T. Mochida, T. Sugawara, The role of hydrogen-bond length in BrHPLN and MeHPLN, J. Korean Phys. Soc. 29 (1996) S436–S439.

[52] N. Kawashima, K. Harada, Recent developments of world-line monte carlo methods, J. Phys. Soc. Jpn. 73 (2004) 1379–1414.

[53] K. Fukui, S. Todo, Order-N cluster monte carlo method for spin systems with long-range interactions, J. Comput. Phys. 228 (2009) 2629–2642.

[54] K. Hukushima, Domain-wall free energy of spin-glass models: Numerical method and boundary conditions, Phys. Rev. E 60 (1999) 3606–3613.